J. COMBIN. MATH. COMBIN. COMPUT. 127a (2025) 8455--8476

Journal of Combinatorial Mathematics
and Combinatorial Computing
www.combinatorialpress.com/jcmcc

Combinatorial Press

Application of computer vision and virtual reality based technology in plant embossing process

Xiaojie Zhao[1,✉]

[1] Hezhou University, Hezhou, Guangxi, 542899, China

ABSTRACT

In this paper, the image parameters are preprocessed by the gray scale histogram statistical image parameters, which reflect the gray scale distribution information of the plant images, using the zero-mean normalization formula. According to different lighting conditions, the plant image is segmented, and the texture feature information in the plant image is extracted by using the improved grayscale covariance matrix. The hyperspectral linear mixing model is constructed, and the MVSA algorithm meta-decomposes the mixing model to solve the solution optimization problem. Using the natural gravity embossing method, produce plant embossed flowers and analyze the features and spectral curves of different parts of the embossed flowers to evaluate the comprehensive use of the embossing method proposed in this paper. The ROI images of 1200 embossed pattern petals were calculated to obtain the sample spectral matrix of embossed petals, in which the reflectance of the central petal was the highest among the three parts at a wavelength of 450 nm, with a reflectance of 0.46487, and then decreased, and then gradually increased to one place after the wavelength was equal to 694, with a reflectance of 0.8. The reflectance of the Shaanxi Weixiang (Weixia), the single side-embossed Yuanbaosi (Yuanbao maple), the hammered elm (fruits), and the pachypodium (Green) obtained a full score of 35 in the comprehensive evaluation after drying, which is a perfect embossed plant material, and all the plant materials embossed using the method proposed in this paper averaged above 30, and the comprehensive effect of plant embossing was good.

Keywords: Zero-mean normalization, Gray scale covariance matrix, Hyperspectral linear mixture model, MVSA algorithm meta-decomposition, Plant embossing

1. Introduction

Computer vision and virtual reality technology are two popular directions in today's science and technology field, and each of them has a wide range of applications in different fields. Computer vision is dedicated to enable machines to read and understand images or videos, and to perform

✉ Corresponding author.
E-mail address: 13878441858@163.com (X. Zhao).
Received 05 February 2024; Revised 12 April 2024; Accepted 05 December 2024; Published Online 15 April 2025.
DOI: 10.61091/jcmcc127a-467

tasks such as image recognition, target detection, and image segmentation by simulating the processing of the human eye [1-4]. While virtual reality is a technology that can create and interact with a virtual world, where users can feel and explore the virtual space in an immersive way. It is important to use both of them in plant embossing process [5-7].

Embossing process is the use of physical and chemical methods, plant materials, including roots, stems, leaves, flowers, fruits, bark, etc. by dehydration, color preservation, pressing and drying to become a flat flower material, after clever ideas, made into a beautiful decorative paintings, cards and daily necessities, such as plant products of a craft [8-10]. The most important feature of embossing technology is that it originates from nature and returns to nature. There are many kinds of plants in nature, and there are more than 500,000 kinds of plants known in nature [11-13]. Embossing process is that these exotic flowers and plants are moved to our living space, so that people can better recognize nature, stay in nature, close to nature. Let people in the love of flowers and cherish the flowers, can see spring flowers in winter, summer to see the winter grass [14-16]. Whether it is used for handicrafts, or applied to home decoration and fashion design, embossing can add unique charm and artistic value to the objects [17-19].

In this paper, the plant images with different color channels are converted into grayscale images by using grayscale histograms, counting their grayscale parameters, applying PCA to unify the image thresholds, determining the best segmentation threshold for the background, and obtaining the plant segmentation images under normal lighting conditions. For plant image segmentation under abnormal light, SLIC algorithm based on K-means clustering is used to preprocess the plant image and realize image segmentation based on color similarity. Roughness and contrast are selected as the feature descriptors of the image sample set and improved according to the actual situation of plants. The plant texture features are extracted using the improved grayscale covariance matrix. The hyperspectral linear mixture model is constructed to calculate the spectral information of the plant, on the basis of which the MVSA algorithm is introduced to analyze the plant form and solve the optimization problem. Through virtual reality technology, the 3D model reconstruction of plants in virtual coordinate system is realized, and plant embossing is produced. Combined with simulation experiments and empirical investigations, the effect of plant embossing under computer vision is analyzed.

2. Computer vision based plant part feature extraction

2.1. Plant image data acquisition

2.1.1. Statistical Parameters of Gray Scale Histograms. Gray scale histogram is widely used in computer vision fields such as image classification field, after the images of different color channels are converted into gray scale images, the gray scale distribution and the degree of lightness and darkness of the image can be reflected by the gray scale histogram [20]. Among them, the most important features of the gray scale histogram are mean, variance, standard deviation, skewness and kurtosis. The above five histogram statistical parameters are selected for the study of plant image classification under different light conditions. The gray scale histogram frequency of image I of size $W*H$ is set to be calculated as shown in equation (1):

$$p(a)=N(a)/(W*H) \tag{1}$$

where $N(a)$ is the sum of the number of pixels on a certain gray level a, the range of gray level a is $[0,255]$, and $p(a)$ is the frequency on a certain gray level with a range of $[0,1]$. For some target pixels in I, their corresponding frequencies in a certain gray scale interval form a contour on the gray scale axis, i.e., they constitute a gray scale histogram, whose distribution represents the statistical characteristics of that target in I. On this basis, some conventional statistical parameters such as mean (μ), variance $\left(\sigma^2\right)$, standard deviation (s), skewness (S) and kurtosis (K) are introduced for analyzing the image, and the calculations are shown in Eqs. (2)-(6):

$$\mu = \sum_{0}^{255} a p(a) \tag{2}$$

$$\sigma^2 = \sum_{0}^{255} (a-\mu)^2 p(a) \tag{3}$$

$$s = \sum_{0}^{255} (a-\mu) p(a) \tag{4}$$

$$S = \frac{1}{\sigma^3} \sum_{0}^{255} (a-\mu)^3 p(a) \tag{5}$$

$$K = \frac{1}{\sigma^4} \sum_{0}^{L-1} (a-\mu)^4 p(a) \tag{6}$$

According to the theoretical knowledge of grayscale histogram, the average level of image brightness is reflected by the mean value, the larger the brightness value represents the larger the mean value, the dispersion of the grayscale distribution in the image is reflected by the variance, if the grayscale in the image deviates more from the mean value of the histogram, the larger the variance is, and vice versa. Standard deviation is similar to variance, skewness reflects the symmetry of the histogram, positive skewness implies a relatively long tail to the right of the mean, while negative skewness is the opposite of positive skewness, kurtosis indicates whether the statistical distribution of the grayscale image is concentrated around the mean.

2.1.2. PCA Uniform Thresholding Image Classification. Due to the different magnitudes of the statistical parameters of the grayscale histogram, if the original parameters are directly used for data fusion to obtain the PCA unified threshold, the larger values of the parameters themselves, such as the mean, variance, and standard deviation, will have a greater impact on the unified threshold, while the smaller values of the parameters themselves, such as the kurtosis and skewness, will have a lesser impact on the unified threshold and affect the classification accuracy of the unified threshold. To address the above problems, the zero-mean normalization formula is used to preprocess the parameters, and the grayscale histogram statistical parameters are scaled to the same specific interval in accordance with the proportion, eliminating the grayscale histogram statistical parameters due to too large a difference in the magnitude leading to the existence of errors in the unified threshold affecting the final image classification, the zero-mean normalization is shown in Equation (7), in which X_j is the jnd grayscale histogram statistical parameters, and μ_j and σ_j are the jth grayscale histogram statistical parameters respectively. Histogram statistical parameters are the mean and variance, respectively:

$$Z_j = \frac{x_j - \mu_j}{\sqrt{\sigma_j}} \tag{7}$$

By preprocessing the statistical parameters of the grayscale histogram through zero-mean normalization, the error problems such as mean, variance, and standard deviation, which have a large impact on the PCA unity threshold, and kurtosis and skewness, which have a small impact on the PCA unity threshold, are effectively eliminated.

2.2. Plant image segmentation under different lighting conditions

2.2.1. Normal light plant image segmentation. Normal light plant image segmentation The plant image used in this paper is a green floral plant image (a part of which will be used for subsequent 3D reconstruction), and in the process of transforming the RGB image into a grayscale image by using a green-sensitive color factor, the grayscale of the color factor corresponding to the image, i.e., the plant region, will be enhanced, and the grayscale of the rest of the region will be weakened, and the grayscale histogram will show a bimodal curve with a distinctive distinction [21]. Therefore, it can be combined with the thresholding method to determine the optimal segmentation threshold for the foreground background to obtain the plant segmentation image.

ExG is derived based on the normalized chromaticity component of the RGB color space, as shown in equation (8):

$$ExG = 2g - r - b \tag{8}$$

where r, g, and b are the color channel components obtained by performing normalization calculations, as shown in Eqs. (9)-(11), respectively:

$$r = \frac{R^n}{\left(R^n + G^n + B^n\right)} \tag{9}$$

$$g = \frac{G^n}{\left(R^n + G^n + B^n\right)} \tag{10}$$

$$b = \frac{B^n}{\left(R^n + G^n + B^n\right)} \tag{11}$$

where, $R^n = \frac{R}{R_{\max}}$, $G^n = \frac{G}{G_{\max}}$, $B^n = \frac{B}{B_{\max}}$ are obtained after regularization of the RGB color space components, R, G, B are the real pixel values in the RGB color space of the image, $R_{\max} = G_{\max} = B_{\max} = 255$.

$MExG$ is improved on the basis of ExG. This factor is experimentally verified to be robust to illumination under good lighting conditions. Therefore, this color factor can also be introduced in this study for grayscaling plant images as shown in Equation (12):

$$MExG = 1.262G - 0.884R - 0.311B \tag{12}$$

The above two color factors are used to preprocess the plant images in grayscale, respectively, and then Otsu is used to determine the optimal threshold T for foreground-background segmentation, as shown in Equation (13):

$$T = \underset{0 \le t \le L-1}{\arg\max}\left[p_a\left(w_a - w_m\right)^2 + p_b\left(w_b - w_m\right)^2\right] \tag{13}$$

where, p_a, p_b are the frequencies of the number of foreground and background pixels compared to the total number of pixels, respectively, and the average gray values of the image, foreground, and background are $w_m = \sum_{i=0}^{L-1} ip_i$, $w_a = \sum_{i=0}^{T-1} i\frac{p_i}{p_a}$, and $w_b = \sum_{i=T}^{L-1} i\frac{p_i}{p_b}$, respectively.

2.2.2. Segmentation of Abnormally Lighted Plant Images. Abnormal light plant image segmentation if the strong light causes white spots to exist on the plant, the use of color factor combined with the threshold method of segmentation will lead to the loss of some of the target information of such images, which affects the quality of the subsequent multi-view plant 3D reconstruction. Therefore, in this paper, on the basis of the obtained research results, the SLIC algorithm based on K-means clustering is used to preprocess such plant images, and the foreground background is divided into super-pixel blocks according to the color similarity between the regional pixels, which can be clustered for the bright spot region, green plant pixels and the background region, respectively. Among them, the color similarity is based on the color factor of the RGB color space of the plant image transferred to the Lab color space and the two-dimensional coordinate space of the image xy together form a five-dimensional feature vector, based on the empirical value of the number of hyperpixel blocks a $M\times N$-sized plant image using SLIC algorithm is divided into K hyperpixel blocks.

Segmented into K hyperimage blocks using the SLIC algorithm, the clustering center $\varphi=\{\varphi_1,\varphi_2,\varphi_3,\dots,\varphi_K\}$ of each hyperimage block will be initialized, and the step size is set to be $S=\sqrt{M\times\frac{N}{K}}$. Starting from φ_1, pixel-by-pixel feature distance computation is performed in the $2S\times 2S$ region around the clustering center and it is judged whether these pixels should be given the same labels as φ_1 until the K-means clustering is satisfied. The feature distance D is calculated as shown in equation (14):

$$D=d_{lab}+\frac{m}{s}d_{xy} \tag{14}$$

The feature distance D is calculated from the distance $d_{lab}=\sqrt{\left(l_p-l_i\right)^2+\left(a_p-a_i\right)^2+\left(b_p-b_i\right)^2}$ between pixel p and cluster center φ_i in Lab color space, and the Euclidean distance $d_{xy}=\sqrt{\left(x_p-x_i\right)^2+\left(y_p-y_i\right)^2}$ between pixel p and φ_i in the xy plane, s is the search step, and m is generally known as the tightness coefficient, which is a weight factor to regulate the Euclidean distance d_{xy}. Ultimately, the hyperpixel blocks are obtained by calculating the clustering of pixels with the distance from the cluster center.

The foreground background is divided into a clustered block, which affects the plant foreground and background segmentation results. According to the principle that SLIC algorithm is implemented based on K-means clustering, the contour coefficient, a common evaluation index for K-means clustering, is used to optimize the division of the number of hyperpixel blocks. The contour coefficient combines two factors of cohesion and separation to evaluate the clustering effect, and is calculated as shown in equation (15):

$$s=\frac{disMean_{out}-disMean_{in}}{\max\left(disMean_{out},disMean_{in}\right)} \tag{15}$$

where $disMean_{out}$ is the distance from a point outside the clustering result to the center of the clustering, and $disMean_{in}$ is the distance from a point inside the clustering result to the center of the clustering. The contour coefficient is in the range of $\left[-1,1\right]$, and tends to be close to 1 to represent a good degree of clustering.

2.3. Computer vision based plant texture and morphological feature extraction

2.3.1. Tamura Texture Characterization. In this paper, we avoided the three linearly correlated features in Tamura features, and finally chose only roughness and contrast as the feature descriptors for the sample set of images in this paper and improved them according to the actual situation of plants [22]. The original algorithm calculates roughness and contrast for the whole image, but in practice, an image often contains foreground and background, and the algorithm itself is more concerned with the texture characteristics of the foreground, without knowing the proportion of foreground and background, if the texture features of the whole image are calculated, then the plant phenotypic texture features that we are interested in may be obliterated in the whole image features.

Roughness Calculating roughness is divided into the following steps:

Step 1: For each pixel point in the image (x, y) calculate the average gray value of the sliding window of size $2^k \times 2^k$ noted as the average intensity $A_k(x, y)$, in this paper the sample image used to calculate the Tamura texture features is an image that has been segmented to retain only the plant part, and the pixel value of the background part is set to $(0,0,0)$. Note (x, y) the number of neighboring pixel points with pixel values not 0 is m, and the roughness is not computed for pixel points that are beyond the sliding window boundaries. The modified average gray scale is shown in Equation (16). In (16), $f(i, j)$ denotes the pixel values of non-background pixel points, $k = 0,1,2\ldots,5$. The modified formula removes the influence of background factors and calculates roughness only for the plant parts we are interested in:

$$A_k(x,y) = \sum_{i=x-2^{k-1}}^{x+2^{k-1}-1} \sum_{j=y-2^{k-1}}^{y+2^{k+1}-1} f(i,j) / m \tag{16}$$

In step 2, for each pixel the average intensity difference between $2^k \times 2^k$ regions where it does not overlap each other horizontally and vertically is calculated separately, as shown in Eqs. (17) and (18):

$$E_{k,k}(x,y) = \left| A_k\left(x+2^{k-1}, y\right) - A_k\left(x-2^{k-1}, y\right) \right| \tag{17}$$

$$E_{k,v}(x,y) = \left| A_k\left(x, y+2^{k-1}\right) - A_k\left(x, y-2^{k-1}\right) \right| \tag{18}$$

Step 3, the calculation of the above equation will produce k set of E values, find the $k_{\max}$ values that can maximize the E values to bring in $S_{bzt}(x,y) = 2^{k_{\max}}$ to get the optimal window for each pixel, and finally calculate the average value of the whole image S_{bzt}. The improvement of roughness in this paper is mainly to count the number of non-zero pixel points in the neighborhood of each plant pixel point, and then use only the non-zero pixel points in the calculation of the average gray scale, so that the roughness of the plant area we are concerned about can be preserved to the maximum.

Contrast ratio is used to count the range of gray level changes in an image, with a larger range of changes representing a larger contrast ratio. In this paper the contrast is calculated using the green component of the segmented image, plants with different aridity levels from the visual point of view firstly their green color distribution is not uniform, and secondly their green color intensity is also significantly different, so extracting features from the green component will have a better differentiation, and the formula for contrast is defined as:

$$F_{com} = \delta / (a_4)^n \tag{19}$$

$$a_4 = \mu_4 / \delta^4 \tag{20}$$

where μ_4 is the fourth order moment and δ is the standard deviation. In this paper, the contrast is similarly calculated by removing the background points, i.e., the points with pixel 0, and disregarding them, and only the plant front points retained after segmentation are calculated.

2.3.2. Improved grayscale covariance matrix characterization. Gray scale covariance matrix (GLCM) is a method used for texture feature extraction, GLCM as a texture descriptor can be viewed as a statistical table of the frequency of occurrence of neighboring pixel intensities in an image [23]. The four directions of $\left[0°,45°,90°,135°\right]$ exist for calculating neighboring pixels in GLCM, and only three directions of $\left[0°,45°,90°\right]$ are finally selected considering the problem of repetitiveness. In order to generate the GLCM matrix, the intensities of all the pixel points in the image need to be mapped to a specified gray level (usually the gray level is greater than 8). The frequency of occurrence of two pixels with gray levels i and j respectively is calculated and the numbers above the rows and columns indicate the 8 gray levels. The original algorithm maps the pixel intensities of the whole grayscale image to the specified gray level, but the samples used in this paper are all plant images, belonging to the same species of plants, and the differences in texture features are much smaller than the differences between different species of objects, even if there is a difference in moisture content. Therefore, in this paper, the range of gray levels is set to 8, while the average minimum value of the green component of plants in all samples is calculated to be recorded as $\overline{g_{\min}}$, and the 8-level mapping is realized by Eq. (21):

$$level\left(x,y\right)=\left(f\left(x,y\right)-\overline{g_{\min}}\right)*\frac{n}{255-\overline{g}_{\min}} \tag{21}$$

The modified gray level mapping formula only considers the green component of the plant image samples, which can describe the change of the intensity of the green component of each pixel point in different directions in a more detailed way. After successfully generating the grayscale co-production matrix, due to the large amount of data in the grayscale co-production matrix, it is generally not directly used as a feature to distinguish the texture, but to construct some statistics based on it as texture classification features. In this paper, the five features extracted based on the generated grayscale co-production matrix are:

The second-order moments are calculated as the sum of squares of all elements in the GLCM, which can reflect the uniformity of the distribution of the G -component of the plant image. From Eq. (22), it can be seen that the value of second-order moments is smaller when the distribution of G components is more uniform, and on the contrary, the value of second-order moments is larger when the distribution of G components is more concentrated in a certain region:

$$ASM = \sum_{i,j-0}^{lovels\ -1} P_{i,j}^{2} \tag{22}$$

Contrast reflects the sharpness of the image and the depth of the texture furrows, through equation (23), it can be seen that the greater the value of the elements away from the diagonal in the GLCM, i.e., the greater the difference between each pair of pixel points and the greater the number of them is the greater the value of the contrast:

$$contrast = \sum_{l,j=0}^{l\ vers\ -1} P_{i,j}\left(i-j\right)^{2} \tag{23}$$

Entropy Value The entropy value is a measure of the randomness of the amount of information contained in an image. The entropy value increases when all values in the GLCM are equal or when the pixel values exhibit greater randomness. Therefore, the entropy value describes the complexity of the distribution of pixel values in an image, and the larger the entropy value, the more complex the image:

$$entropy = -\sum_{i,j=0}^{lovects-1} P_{i,j}\log P_{i,j} \tag{24}$$

The IDM inverse disparity is used as a measure of how much local texture variation there is in the image, as shown in equation (25), where a larger value indicates a lack of variation between different regions of the image texture and a more uniform local texture:

$$IDM = \sum_{i,j=0}^{leverk\text{-}1} \frac{P_{i,j}}{1+(i-j)^2} \tag{25}$$

Discrepancy works similarly to contrast as shown in equation (26) is mainly used to measure the difference in pixel values in an image:

$$Dis = \sum_{i,j=0}^{love\ k-1} P_{i,j} |i-j| \tag{26}$$

Hyperpixel processing is to divide the image into small regions, each small region is called a hyperpixel block, and the hyperpixel block belongs to only one class of objects in the image, the hyperpixel processing usually starts from a simple initial division, and then enters into the iteration and adjustment, and completes the division of the region after a number of cycles. The basic steps are:

$$E_f = \sum_{i=0}^{m} \sum_{j=0}^{n} f(i,j)^2 / (m*n) \tag{27}$$

2.3.3. Morphological characteristics:

1) Convert the RGB image to CIE-Lab space, assuming that K superpixel block is generated and the image size is $M \times N$ (648×432 in this paper), then the edge length of each superpixel block is:

$$l = \sqrt{(M \times N)/K} \tag{28}$$

2) Initialize the seed points (clustering centers), and uniformly distribute the seed points according to the preset number of superpixels and the calculated pixel block size in step (1). Assign labels to each pixel block with labels of the seed points.

3) Calculate the gradient values of all pixel points in the neighborhood of $n \times n$ (usually $n = 3$) of the seed point of each pixel block, and find the pixel point with the smallest gradient to be reassigned as the seed point, to avoid the seed point from falling on the boundary with large gradient.

4) Reassign labels to each pixel point by K-means clustering within the neighborhood of each seed point, the distance in clustering is calculated as shown in Eqs. (29) to (31), and the neighborhood search range is $2l \times 2l$:

$$D = \sqrt{\left(\frac{d_c}{m}\right)^2 + \left(\frac{d_s}{l}\right)^2} \tag{29}$$

$$d_c = \sqrt{(l_j - l_i)^2 + (a_j - a_i)^2 + (b_j - b_i)^2} \tag{30}$$

$$d_s = \sqrt{(x_j - x_i)^2 + (y_j - y_i)^2} \tag{31}$$

where d_c represents the color distance, d_s represents the spatial distance, where m is the balance parameter, which is used to measure the ratio of pixel value and spatial information in the similarity measure, the larger the value of m is, the larger the weight of spatial distance in measuring the similarity distance between two pixels, and its value range is usually $[1,40]$. Considering that the application dataset in this paper is a binary image segmented to retain only the foreground of the plant and the black background, it is not necessary to use the CIE-Lab space when using hyperpixel clustering. Considering that the application dataset in this paper is a binary image segmented to retain only the foreground of the plant plant and the black background, the categories in the image are simple and the boundary between the plant plant and the black background is clearer, there is no need to use the CIE-Lab space when using the hyperpixel clustering. In this paper, the color distance and the final total distance are modified as shown in Eqs. (32)(33), the color distance metric uses the difference of the pixel values of the binary pixel points, and the squaring and squaring operations of the total distance are omitted in order to reduce the computational effort. In this paper, the number of hyperpixels is set to 1000, and the initial side length of each hyperpixel is 16 as calculated by Eq. (28). Through experimental comparison the hyperpixel blocks obtained when $m = 20$ are uniform and regular in shape therefore the value of m is set to 20:

$$D_c = \left| I_k - I_i \right| \tag{32}$$

$$D_s = \frac{D_c}{m} + \frac{D_s}{l} \tag{33}$$

2.4. Meta-decomposition based on hyperspectral image blending

2.4.1. Hyperspectral linear mixing models. Figure 1 shows a schematic of the hybrid image element model for hyperspectral images. Spectral imaging technology has been widely used in the fields of agriculture, environmental monitoring, mineral exploration, military detection, etc. However, due to the low spatial resolution of imaging sensors, the presence of mixing effects during atmospheric transmission, and the mixing effect of the sensors themselves, it often occurs that there are a variety of different features within a single image element, which leads to the existence of hyperspectral images with the problem of mixed image elements [24]. It mainly occurs at the boundary of features, and the existence of mixed pixels is one of the main factors affecting the classification accuracy of feature recognition, especially on the classification and recognition of linear features and fine features. Mixed pixel decomposition of hyperspectral images has two basic purposes: to determine the basic types of features that make up the mixed pixel, i.e., the process of extracting the end-elements, and the pixel that contains only one type of feature is called a pure pixel, which can be used as the end-element of one type of feature, and thus the end-element can represent the spectral information of one type of feature. Calculate the proportion of each end-element in the mixed image element, i.e., the abundance inversion process, and the abundance of all the features within the image element sums to one.

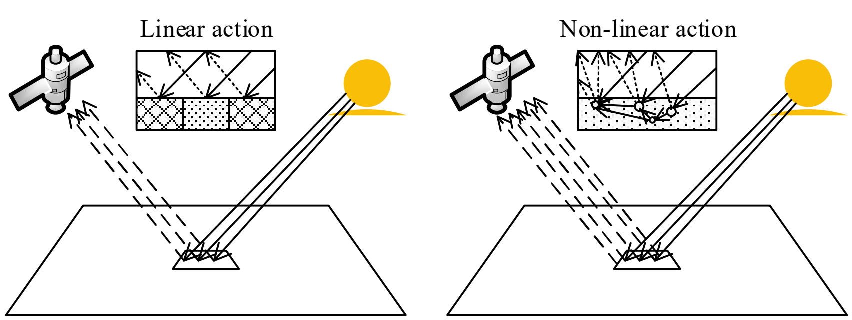

Fig. 1. Hyperspectral image hybrid pixel model

Assuming L-band hyperspectral data containing $m \times n$ image element (m, n, and L are the spatial length, width, and number of bands of the hyperspectral data cube, respectively), and that the data contains M kinds of end-elements, the linear mixing model can be expressed as:

$$r_i = \sum_{j=1}^{H} e_j \alpha_{ij} + \varepsilon_j \tag{34}$$

where e_j is the end-element spectrum, α_{ij} is the weight of e_j in r_i the corresponding geographic region, i.e., the abundance, and ε_j is the random noise of the data in a vectorized representation of the hyperspectral data cube linear mixture model:

$$R = EA^T + \varepsilon \tag{35}$$

where R is the hyperspectral image data, E is the end-element spectrum, A is the corresponding abundance matrix, ε represents the random noise matrix, and each column of R and E represents an image element. The model obeys the following constraints:

1) The number of end elements is not greater than the number of bands and the number of image elements, $M \le \min\{L, m*n\}$.

2) The end elements are linearly uncorrelated with each other, i.e. $rank(E) = M$.

3) The set of end-elements is a subset of the set of image elements, i.e. $\{e_j\}_{j=1}^{M} \subset \{r_i\}_{i=1}^{m*n}$, i.e. there exists at least one set of image elements such that $r_j = e_j + \varepsilon_j$.

4) The abundance matrix A in the mixed image elements should satisfy the constraints that the sum of the abundances is 1 and that all abundances are non-negative, i.e:

$$\sum_{i=1}^{U} A_i = 1, 0 \le A_i \le 1, \mathrm{i} = 1, 2 \cdots, p \tag{36}$$

The abundance estimation process after end-element extraction is actually solving the optimal solution to the following problem:

$$\min \left\| R - EA^T \right\|_2^2 \tag{37}$$

2.4.2. MVSA Algorithm. MVSA algorithm is an unsupervised hyperspectral image hybrid pixel decomposition algorithm, called the minimum volume monosome analysis algorithm, through the method of expanding from the inside to the outside to find the smallest volume of monomorphs that can include all pixel points, so as to extract the endmembers of the hyperspectral image, before the endmember extraction, it is also necessary to determine the number of endmembers m, because the number of endmembers extracted by the MVSA algorithm can only be the same as the number of bands of the hyperspectral image L, Therefore, before using the MVSA algorithm to extract the endmembers, the hyperspectral image needs to be dimensionally reduced, so that the image spectral band L is the same as the number of endmembers to be extracted m, because the minimum volume monomorph algorithm is not a convex optimization solution solving algorithm, so the algorithm only looks for a good enough suboptimal solution in a large number of local optimal solutions, not the global optimal solution, when the number of end members extracted by the image spectral band $L =$ is m, the compressed image end member set is a square matrix and all the end members in the set are linearly independent of each other, The MVSA algorithm solves the optimization problem:

$$\hat{S} = \arg\min_{M} \left\{ \left| \det(S) \right| \ s.t: S^{-1}X \ge 0 1_L^T S^{-1}X = 1_1^T \right. \tag{38}$$

where $\det(S)$ is the determinant of S, which is the volume of the monomorphism that satisfies the condition:

$$\det(S) * \det(S^{-1}) = 1 \tag{39}$$

Thus equation (39) can be converted into the following form:

$$\hat{S}^{-1} = \arg\min_{M} \left\{ \left| \det\left(S^{-1}\right) \right| \right\} \; s.t \; : S^{-1}X \geq 0 1_1^{\bullet}\; S^{-1}X = 1_1^{\bullet} \tag{40}$$

The problem of extracting end-elements can be converted into a problem of solving S^{-1} by Eq. (40), where each image element exists in a subspace of S. Assuming that the hyperspectral image contains $m \times n$ image elements, there must exist a square array $X_{il} = \left\{x_{j1}, x_{i2}, \cdots, x_{ja}\right\}$ consisting of m linearly unrelated column vectors $\left\{x_{lk}\right\}_{k=1}^{M}$ in the hyperspectral data, and thus this optimization problem can be solved by the Stepwise Quadratic Programming (SQP) method:

$$Q = SQP\left[f, Q_0, X, 0, 1_L^T, 1_s^T \left(X_s\right)^{-1}, g, H\right] \tag{41}$$

where: f is the objective function, g is the gradient value of f, H is the Hessian matrix of f, and Q_0 is the initial value of the iteration.

3. 3D reconstruction of plant models based on virtual reality technology

3.1. Model construction in virtual reality

Currently, 3D models for virtual reality are often obtained by the following three methods, the first way using modeling software to construct the 3D model, the second way by instrumentation to obtain the 3D model, and the third way using images or videos to reconstruct the scene 3D model [25].

In the rotation relation, several coordinate transformations need to be taken into account.

In the ideal case, $\bar{v}_v^1$ and $\bar{v}_v^2$ are the relationship of rotation only around the 2-axis, then $R1$ can be expressed as the rotation performed around the ground law, that is, the rotation performed in the direction of the 2-axis after the change of the coordinate system mentioned above, so $R1$ can be written as:

$$RI = \begin{bmatrix} \cos\theta & -\sin\theta & 0 \\ \sin\theta & \cos\theta & 0 \\ 0 & 0 & 1 \end{bmatrix} \tag{42}$$

where θ is the angle of clockwise rotation around the 2-axis direction.

Using the equation:

$$\begin{bmatrix} v_x^1 \\ v_y^1 \\ v_z^1 \end{bmatrix} = \begin{bmatrix} \cos\theta & -\sin\theta & 0 \\ \sin\theta & \cos\theta & 0 \\ 0 & 0 & 1 \end{bmatrix} \begin{bmatrix} v_x^2 \\ v_y^2 \\ v_z^2 \end{bmatrix} \tag{43}$$

It is possible to solve the rotation matrix $R1$.

But in practice, $\bar{v}_v^{-1}$ and v_v^{-2} do not necessarily have only the Z axis as the axis of rotation, i.e., $v_z^1 \neq v_x^2$, then the rotation relationship of $R1$ is not sufficient. So consider the actual relationship between $\bar{v}_v$ and $v_v{}^2$ before doing $R1$ the rotation.

In the following, a rotation transformation is needed to take the direction of v_v as the Z-axis direction of the new coordinate system, i.e., the current coordinate system with the ground normal as the 2-axis is rotated to become a new coordinate system with v_v^{-1} as the 2-axis. In this paper, it is assumed that such a rotation is a rotation around the X-axis and Y-axis of the current coordinate system respectively, so this rotation matrix $R2$ can be written as:

$$R3=\begin{bmatrix}\cos\kappa & \sin\omega\sin\kappa & \cos\omega\sin\kappa\\ 0 & \cos\omega & -\sin\omega\\ -\sin\kappa & \sin\omega\cos\kappa & \cos\omega\cos\kappa\end{bmatrix} \tag{44}$$

where ω is the angle of rotation clockwise about the X-axis direction and κ is the angle of rotation clockwise about the Y-axis direction. To solve for ω and κ, consider the following geometric equations:

$\overline{v}_v^{-1}=R3^{-1}\begin{bmatrix}0\\0\\1\end{bmatrix}$ and $\overline{v}_v^{-1}$ can be obtained by rotating the Z-axis about the X-axis and the Y-axis, so that its counter-rotation is the required $R3$:

$$\begin{cases} v_x=\cos(-\omega)\sin(-\kappa)\\ v_y=-\sin(-\omega)\\ v_z=\cos(-\omega)\cos(-\kappa)\end{cases} \tag{45}$$

It can be assumed that a rotation angle κ around the Y-axis from $-\frac{\pi}{2}$ to $\frac{\pi}{2}$ must, for a rotation angle ω around the X-axis, have values from $-\frac{\pi}{2}$ to $\frac{3\pi}{2}$.

The last coordinate transformation is aimed at solving a rotation matrix R4 that maximizes the overlap of the set of leaf points of viewpoint 2 with the set of leaf points of viewpoint 1. What is to be solved is how viewpoint 2 undergoes a rotational transformation R4 around the stem to have maximum overlap with the counting blades of viewpoint 1.

Emulating the solution of the R1 matrix, there can be:

$$R4=\begin{bmatrix}\cos\theta' & -\sin\theta' & 0\\ \sin\theta' & \cos\theta' & 0\\ 0 & 0 & 1\end{bmatrix} \tag{46}$$

We perform a rotation test around the stem direction for viewpoint 2. We set the starting rotation value to $-\pi$, the step size to $\pi/72$, and measure the distance d between the two viewpoints within the rotation 2π. Here d we define:

$$d=Arg\min\sum \min Dist\left(X_2,\{X_1\}\right) \tag{47}$$

For any rotation angle, each point in viewpoint 2 finds its nearest point in viewpoint 1 and calculates its distance. The sum of the distances of each point in viewpoint 2 from viewpoint 1 is used as the distance between the two viewpoints at that rotation test angle. When the distance between the two viewpoints reaches a minimum value at a certain rotation test angle θ, θ in the rotation relation $R4$ between the two viewpoints becomes the rotation test angle at that time.

So by the above illustration, the final rotation matrix R from viewpoint 2 to viewpoint 1 can be obtained:

$$R=\begin{cases} R3^{-1}\cdot R4\cdot R3\cdot R1,\ if\ v_z^1=v_z^2\\ R3^{-1}\cdot R4\cdot R3\cdot R2\cdot R1,\ if\ v_z^1\neq v_z^2\end{cases} \tag{48}$$

3.2. Triangular piecewise treatment of scattered points

For each region, a different topology is fitted. For petals the scattered points need to be fitted to a surface without thickness. A spline interpolation algorithm is used, which not only effectively removes noise, but also makes full use of the scattered points formed by multiple views.

Basic notation and problem formulation:

$\Omega = \{(x, y) | 0 \le x < m, 0 \le y < n\} XY$ a rectangular definition domain in the plane, a set of scattered points $P = \{(x_c, y_c, z_c)\}$, $(x_e, y_c) \in \Omega$, f used to approximate the uniformly bi-tertiary B spline function of the arithmetic messy data P, determined by a control grid Φ. It may be useful to set Φ to be the lattice of $(m+3)\times(n+3)$, $\forall \phi_{ij} \in \Phi$, ϕ_{ij} the projection $\in \{(i, j) | -1 \le i \le m+1; -1 \le j \le n+1; i, j \in Z\}$ to Φ:

$$\begin{aligned} f(x, y) &= \sum_{k=0}^{3}\sum_{l=0}^{3} B_k(s) B_1(t) \phi_{(i+k)(j+1)} \\ i &= \lfloor x \rfloor - 1, j = \lfloor y \rfloor - 1, s = x - \lfloor x \rfloor \\ t &= y - \lfloor y \rfloor \end{aligned} \tag{49}$$

B_k, B_l are uniformly 3 times B spline basis functions. Thus the problem of approximating P with f is transformed into a problem of determining the z value of Φ.

The determination of the control grid Φ:

$\forall (x_c, y_c, z_c) \in P$, $f(x_c, y_c)$ is related only to its neighboring 16 control points. It may be useful to set $1 \le x_c$, $y_s \le 2$ known from equation (50):

$$z_c = f(x_c, y_c) = \sum_{k=0}^{3}\sum_{t=0}^{3} w_{kl}\phi_k, w_{kl} = B_k(s)B_l(t) \tag{50}$$

There are many sets of values of ϕ_{kl} that satisfy equation (50), and a least squares $\min \sum_{k=0}^{3}\sum_{l=0}^{3} {\phi_{kl}}^2$ is done to minimize the distance between f and 0 on the domain of definition Ω. Using the pseudo-inverse yields the solution as:

$$\phi_{tl} = \frac{w_{ki} z_c}{\sum_{k=0}^{3}\sum_{l=0}^{3} w_{ch}^2} \tag{51}$$

The f' thus obtained is interpolated to (x_c, y_c, z_c) with smooth decreasing around it. Now consider all the data points in P. Each point is determined by equation (51) to have 16 neighboring controls. However the data points will have common controls if they are closer to each other.

To solve this multiple assignment problem, for each control point all data points falling in its 4*4 neighborhood constitute its proximity point set (ϕ_{ij}). Let P_{ij} be the set of proximity points $P_{ij} = \{(x_c, y_c, z_c) \in P | i-2 \le x_c < i+2, j-2 \le y_c < j+2\}$ of control point ϕ_n, and for ding each (x_c, y_c, z_c), Eq. (51) gives ϕ_{ij} a different value ϕ_c:

$$\phi_c = \frac{w_c z_c}{\sum_{a=0}^{3}\sum_{k=0}^{3} w_{ab}^2} \tag{52}$$

$$w_c = w_{kl} = B_k(s)B_l(t), k = (i+1) - \lfloor x_c \rfloor, l = (j+1) - \lfloor y_c \rfloor \tag{53}$$

Finally, ϕ_{ij} can be determined from $\min \sum_c (w_c\phi_{ij} - w_c\phi_c)^2$:

$$\phi_q = \frac{\sum_c w_c^2 \phi_c}{\sum_c w_c^2} \tag{54}$$

When there are several points in P, Eq. (54) is the least squares solution to minimize the local approximation error, and when there is only one point in P, Eq. (54) reduces to Eq. (52), with no approximation error, and when there are no points in P, ϕ_n does not contribute to $f\left(x_c, y_c\right)$, i.e., any value of $\forall\left(x_c, y_c, z_c\right) \in P$, ϕ_y does not affect the approximation error, and so it is generally taken to be zero.

4. Plant embossing production

4.1. Flower Selection

General embossing covers various types of materials such as vines, stems, leaves, flowers, roots, bark, seeds, fruits, tendrils, etc., and the most frequently used are flowers and leaves. When choosing flowers, usually the artistic effect of plant pressed flower works depends on different factors such as flower form, texture and color. For example, in choosing flower color, the pigment content of plant petals varies, of which the physical and chemical properties of intracellular pigments are more significant, especially the internal structure and surface of the petals will form physical changes, and thus form colorful flower colors. Plant embossing requires the petals to be brightly colored and to maintain their original color after pressing, so plant embossing producers need to understand the flower color scientifically and constantly enrich their theoretical and practical experience. Based on the practice of flower pressing, it is known that blue, golden yellow, orange-red and purple plant flowers are relatively simple to press, and it is also easier to keep the color. White, bright yellow, red, pink and other flowers and their petals contain more water, it is difficult to maintain the color.

When choosing flower colors, if the type of flower material is the same, then you can collect different flower colors of that type of flower material, for example, beauty cherry, rose and hydrangea which are popular in the flower market are available in many colors. From the picture, it can be found that pressed flower works can present different artistic effects due to multiple flower colors. When pressing the same type of flower materials, priority will be given to compound or variegated flowers to enhance the sense of hierarchy of the pressed flower works. When choosing flower shapes, whether or not the pressed flower works can achieve the expected artistic impact depends entirely on the beauty of the flower forms. Therefore, when choosing flower shapes, we select small and medium-sized single-petal flowers or double-petal flowers such as delphinium, hydrangea, cosmos, white crystal chrysanthemums, and other small and medium-sized single-petal flowers, whose flower shapes are of moderate size, simple structure, and good planar forms. If the flower has more petals, it can be peeled off and then disassembled and pressed, in which bag-shaped flowers, tube-shaped flowers and butterfly flowers are difficult to be used as plant pressing material.

4.2. Flower Pressing

4.2.1. Embossing tool selection. Currently there are two types of embossers, the microwave and the dry plate embosser, which are widely used in plant embossing, and the selection of the tool for the specific embossing needs to be based on the experience gained from time to time. Most of the plants are suitable for dry plate embossing, while the European red maple is suitable for microwave embossing, which can keep the color of the flowers. Hydrangeas are unique in that they do not tolerate high temperatures and cannot be pressed with a microwave press. For flowers that are difficult to dehydrate, we can use the combination of drying board and microwave embosser to improve the efficiency and quality of drying. For the dry climate of the north and other areas, in the fall there will be a large discoloration of the leaves fall, just use the home of the old magazines, used printing paper, old newspapers, blotting paper or old books can be pressed with less water content of the autumn leaves.

4.2.2. Natural gravity embossing method. The climate is dry in autumn and winter in the north, many roads will drop colorful leaves with little water content and different shapes, if there is a lack of microwave embossers and drying boards, you can use newspaper, cotton paper, toilet paper and other conventional absorbent paper or thick books, boxes, stones, bricks and other heavy weight to press the flowers, and you can still get flat and dry flower materials. In several layers of blotting paper placed on the treated flowers, and then placed 1 layer of flowers with several layers of blotting paper, and finally placed 1 layer of flowers, repeated operations covered with bricks and heavy pressure, the embossed works placed in a dry and ventilated place, in the process of changing the blotting paper, 6d after the basic press dry material.

4.2.3. Plant embossing production based on computer vision and virtual reality technology. Using the computer vision technology designed in this paper, the texture extraction and morphology extraction of the plant part features are carried out to ensure the beauty of the finished plant embossing product. At the same time, combined with virtual reality technology, for each region of the plant 3D model, according to different topological structures for fitting, the scattered points of the petals are fitted to the surface without thickness, to ensure that the plant embossed finished product in multiple angles of the best presentation.

5. Results and analysis

5.1. Classification of plant embossed parts based on computer vision technology

5.1.1. Extraction of plant embossing features from different parts of the plant. Figure 2 shows the relative geometric feature parameters of different parts of the Pat Sinensis flower, using computer vision for image acquisition, the original image of fresh tobacco is a 24-bit true color image with a resolution of 1288 × 964 pixels. A total of 1200 images used for embossing Pat Sinensis flowers were collected, 400 pieces for each different part, and the Pat Sinensis flower samples were classified and labeled according to the part to which the Pat Sinensis flowers belonged, with the lower part (X) labeled as 1, the middle part (C) labeled as 2, and the upper part (B) labeled as 3.

Based on the original images of Patagonian flowers collected by computer vision technology, the shape feature parameters of Patagonian flowers were extracted. Gray scale binarization is performed on the original image to realize the separation of petals and background in the image, and then the Canny operator is used to perform edge extraction on the contour features of the Patisserie flower, construct the outer rectangle of the petal contour, and extract the edge feature parameters of the petals.

The relative geometric feature parameters of the petals of different parts of the flower are shown in Figure 2. It can be seen that the differences in narrowness and rectangularity between the petals of different parts of Patagonian flowers are more significant, and the values of the three parts of the petals almost do not appear to overlap, as far as narrowness is concerned, the narrowness of the petals of different parts of the flower is different, with the upper part of the interval between (0.2,0.3), the middle part of the interval between (0.29,0.4), and the lower part of the interval between (0.35,0.5).

There was less variability in roundness and leaf width axis, and more dispersion in position at petal maximum, which was not significant.

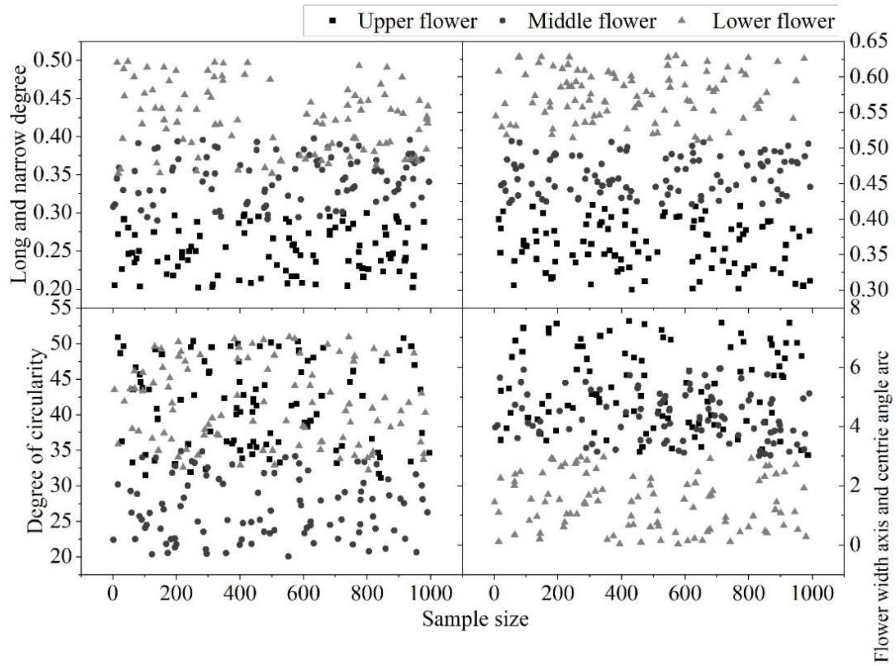

Fig. 2. The relative geometric characteristics of the eight fairy flowers in different parts

5.1.2. Results of plant embossing site discrimination based on flower shape characteristics. The extracted flower shape and texture feature data are randomly selected into the training set and test set according to the ratio of 4:1. The training set samples consist of 356 upper, 356 middle and 356 lower samples, which are used for the construction of the part recognition model, and the remaining petals are used as the prediction set samples, which contain 44 upper, 44 middle and 44 lower samples, which are used to test the prediction ability of the model. In the classification discrimination, if there is a non-integer case then according to the threshold discrimination, define the discrimination rule of the model as follows: if the predicted category value satisfies 0.5 ⩽ predicted category value < 1.5, it is judged to be the lower part. If meet 1.5 ⩽ predicted category value < 2.5, judged as the middle leaf. If 2.5⩽predicted category value <3.5 is satisfied, it is judged as upper leaf. If the predicted category value ⩾ 3.5 or the predicted category value < 0.5, it is judged as an abnormal sample.

In order to avoid the impact of data redundancy on the efficiency and accuracy of the classification model caused by too high a number of dimensions, the extracted data of the 10 shape features were downscaled using principal component analysis (PCA). Figure 3 shows the results of principal component analysis for the 10 contour feature parameters of the fresh petal samples. The first 2 principal component variables can explain 89.47% (PC-1 65.15%, PC-2 24.32%) of the information contained in the 10 shape feature data, and all 3 parts show better clustering effects, indicating that the shape feature data have better results for petal part classification prediction. Based on the loading values of the 10 shape features in the first two principal component variables, the shape features with lower relevance to part classification were eliminated, and finally the first three shape feature parameters of narrowness, rectangularity, roundness, and the first two principal component variables of PCA screening, which had a greater contribution to part classification, were selected as the shape feature variables, totaling five features.

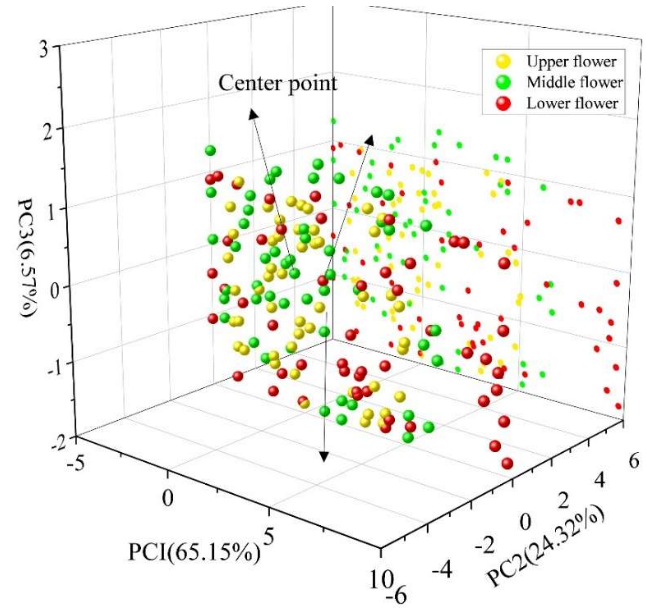

Fig. 3. The main component analysis results of 10 profiles of flower flap samples

5.1.3. Spectral curves of embossing in different parts of the body. The original hyperspectral images were corrected in black and white using the hyperspectral linear mixing model. The original fresh petal hyperspectral image data is a three-dimensional data block, and Fig. 4 shows the spectral curves of different parts of the petals. By observing the collected hyperspectral images, the boundaries between the petals and the background are clear and easy to be segmented, so it is very important to use the threshold segmentation method to segment the fresh petals and the background, and to realize the binarization of the fresh petal image through the corrosion expansion process, and to take the whole petal region as a ROI, and to calculate the average spectral reflectance of all the pixel points within each ROI as the spectral value of each petal sample. The average spectral reflectance of all pixel points in each ROI was calculated as the spectral value of each petal sample, and an average spectral curve representing the petal sample could be obtained for each petal. The same steps were repeated for the ROI images of three parts totaling 1200 petals to obtain a 1200*356 spectral matrix of petal samples, and three peaks appeared in the spectral curves of different parts, in which the reflectance of the middle petal was the highest among the three parts at a wavelength of 450 nm at a reflectance of 0.46487, and then there was a decrease in the reflectance, which was lower than that of the lower part. After the wavelength equal to 694 nm gradually rose to one place and the reflectance reached 0.8.

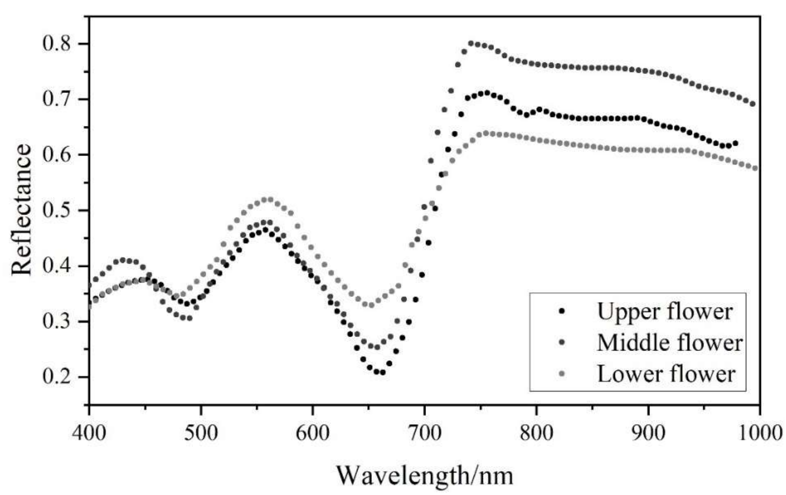

Fig. 4. The spectral curve of the petals of different parts

In summary, this subsection verifies the usability of computer vision technology in plant embossing process, and the simulation experiment results confirm the accuracy of computer vision technology in extracting and identifying the embossed parts of the plant and obtaining the embossed spectral curve information to realize the visualization and analysis of embossing process data. Next, the technology proposed in this paper is applied to the actual plant embossing process, and the practicality of the algorithm is empirically examined.

5.2. Evaluation of the comprehensive effect of plant embossing

5.2.1. Green plant embossing effect. Using the computer vision technology and virtual reality technology designed in this paper, the embossed material was firstly feature extracted and part identified to obtain the basic information of the embossed material to ensure the final presentation effect of plant embossing. Then, according to the production process of plant embossing proposed in Chapter 4, the production of plant embossing was completed. Table 1 shows the effect of green plant embossing, among 20 kinds of green plant materials, 13 kinds basically keep the original color after drying. The main pigment of green plants is chlorophyll light stability and heat stability is strong, not easy to be decomposed, and in the neutral or weak acid and alkali conditions, chlorophyll is more stable, so the green plants before and after the drying of color retention is good. Among these plants, Shaanxi Weihua, Yuanbao Maple, Buxus, Weeping Willow, Pink Dumpling, and SPARKLING Flower are flowers or inflorescences, which fill the more scarce pool of green pressed flowers, Hammer Elm is pressed with fruits, and the rest of the pressed are the green leaves of the plant. Shaanxi Weeping Spear, single side-pressed Genbaku Maple, Hammer Elm (fruit), and Pachysandra (green) received perfect scores (35) in the overall evaluation after drying, making them perfect embossed plant material. Most of the leaves were less tough after drying, and the thickness of single positively pressed Genbaku maple was thinner after drying.

Different pressing methods were adopted for SPARKLE FLOWER and METAPLANE for the characteristics of green plants, and according to Table 1: different pressing methods had less effect on the drying effect of SPARKLE FLOWER, and METAPLANE with single positive pressing had thinner thickness after drying than that of single side pressing.

Table 1. Green plant effect

Plant name	Suppression mode	Pressed texture	Points
Euonymus shaanxiensis	Inflorescence pressure	· Strong toughness, opaque, flat, moderate thickness	35
Acer truncatum	Single lateral pressure	· Strong toughness, opaque, flat, moderate thickness	35
Elm(fruit)	Positive pressure	· Strong toughness, opaque, flat, moderate thickness	35
Hydrangea (green)	· Single positive pressure	· Strong toughness, opaque, flat, moderate thickness	35
Snake berry (leaf)	Positive pressure	Strong toughness, opaque, flat, moderate thickness	34
Spiraea (leaf)	Positive pressure	Strong toughness, opaque, flat, moderate thickness	33
Willows(inflorescence)	Inflorescence pressure	Strong toughness, opaque, flat, moderate thickness	33
Tamarisk	Positive pressure	Strong toughness, opaque, flat, moderate thickness	32
Lysimachia japonicum	Positive pressure	Strong toughness, opaque, flat, moderate thickness	32
Acer truncatum	·Single positive pressure	Strong toughness, opaque, flat, thin e	32
Dough (first flower)	· Single positive pressure	Strong toughness, opaque, flat, moderate thickness	31
Arborvitae orientalis	Positive pressure	Strong toughness, opaque, flat, thick	31
Chaste tree	Positive pressure	Relatively crisp, opaque, flat, moderate thickness4	31
Stachyurus	Inflorescence pressure	Relatively crisp, opaque, flat, moderate thickness4	30
	Single lateral pressure	Relatively crisp, opaque, flat, moderate thickness4	30

5.2.2. Embossing material evaluation score. According to the scoring standard for each index of the pressed material to score, calculate the average value of each factor as its most score, based on the scoring standard and the weight of each influential factor to calculate the comprehensive score value of the embossed material:

$$N_j = \sum_{i=1}^{n} W_{ij} R_{ij} \tag{55}$$

where: N_j is the final total score of a plant embossing material, j indicates a plant embossing material, i indicates a certain evaluation factor, W_{ij} indicates a certain scoring index weight of a plant embossing material, and R_{ij} indicates the score of that evaluation index of a plant embossing material.

The comprehensive score of each plant was calculated according to formula (55) Table 2 shows the evaluation scores and grades of embossed materials. K-Means clustering analysis was used to classify the embossed materials of 56 kinds of plant flowers after pressing, and they were divided into four grades of Ⅰ, Ⅱ, Ⅲ and Ⅳ in order from the best to the worst, which corresponded to the clustering centers of 2.915, 2.654, 2.362 and 1.915, respectively, of which there were 28 kinds of Ⅰ grade varieties, accounting for 50%, and 50% of the varieties, which corresponded to the cluster centers of 1.915. 28 varieties, accounting for 50%, 9 varieties of grade II, accounting for 16.07%, 15 varieties of grade III, accounting for 26.79%, and 4 varieties of grade IV, accounting for 7.14%. The top ranked pressed flowers in the four grades were Gerbera daisies (yellow), carnations (purple), Star of Bethlehem, and pansies, with pressed scores of 2.9455, 2.6574, 2.5045, and 2.2364 respectively.

Table 2. Scoring and grading of emboverment materials

Name	Mark	Lv.	Name	Mark	Lv.
Gerbera (yellow)	**2.9455**	I	Carnation (Purple)	**2.6574**	II
Gerbera (Orange)	2.9264	I	Hibiscus	2.6564	II
Red flower	2.9078	I	Dahlia	2.6482	II
Sunflower	2.9048	I	Chamomile	2.6154	II
Cinquechrysanthemum	2.8154	I	Violet	2.5846	II
· Carnation (yellow)	2.8766	I	Wenxin Orchid	2.5769	II
Embroidery - Ball	2.8615	I	Rose (red).	2.5498	II
Carnation (powder)	2.8348	I	Vermilion	2.5264	II
Bougainvillea	2.8304	I	Vetch	2.5169	II
Rose (Orange)	2.8234	I	Star of Bethlehem	**2.5045**	III
Baby's Breath	2.8178	I	Abel	2.4978	III
Yunnan Suxin	2.8143	I	Six flowers	2.4594	III
Plumeria	2.8036	I	Solidago canadensis	2.4588	III
Rose (white)	2.8015	I	Dendrobium	2.4368	III
Chinese rose (yellow)	2.7936	I	Periwinkle	2.4154	III
Yucca	2.7815	I	Purple velvet sage	2.3945	III
Bamboo	2.7624	I	Lily	2.3348	III
Stone ·	2.7611	I	Red orchid	2.3154	III
Gerbera (red)	2.7602	I	Big Flower Whelan	2.3064	III
Crape Myrtle (Purple)	2.7415	I	Chrysanthemum (white)	2.3015	III
February Orchid	2.7405	I	Autumn chrysanthemum (purple)	2.2678	III
Sleeping lotus	2.7403	I	Autumn chrysanthemum (white)	2.2644	III
Green Onion Orchid	2.7396	I	Lisicodon grandiflorum (Purple)	2.2425	III
Carnation (red))	2.7154	I	Chrysanthemum (yellow)	2.2374	III
Cuckoo	2.6974	I	Pansy	**2.2364**	IV
Golden Daisy	2.6715	I	Lisicodon grandiflorum (green)	2.2154	IV
Japanese evening cherry	2.6706	I	Canna	2.1548	IV
Crape myrtle(Red)	2.6484	I	Chrysanthemum (powder)	1.9784	IV

6. Conclusion

In this paper, we use gray scale histogram to count the plant image parameters and classify the images by PCA unified thresholding method. The plant images are segmented according to different lighting conditions. Based on computer vision technology, plant texture and morphological features are extracted. Adopt hyperspectral linear mixing model, decompose the elements of hyperspectral image mixing, and realize 3D reconstruction of plant model in virtual reality technology.

Determine the embossing materials and tools, and make plant embossing by natural gravity embossing method. The geometric feature parameters of different parts of the plant embossed flowers were extracted, and the differences in narrowness and rectangularity between petals of different parts of Patagonian flowers were more significant, for narrowness, the narrowness interval of the upper petals was between (0.2,0.3), the middle was between (0.29,0.4), and the lower part was between (0.35,0.5). The variability in roundness and leaf width axis was low, and the dispersion of the position at the petal maximum was high and not significant.

Using principal component analysis, the extracted 10 shape feature data were downscaled, and the first 2 principal component variables could explain 89.47% (PC-1 65.15%, PC-2 24.32%) of the information contained in the 10 shape feature data, and the three parts showed a better clustering effect, which indicates that the shape feature data extracted by the model has a better effect on the prediction of petal part classification.

K-Means clustering analysis was used to classify the pressed flower materials after 56 plant flowers were pressed, and the first ranked pressed flowers in the four classes were Gerbera daisy (yellow), carnation (purple), Star of Bethlehem, and pansy, with pressed scores of 2.9455, 2.6574, 2.5045, and 2.2364, respectively, which showed a better overall effect of pressed flowers.

Funding

"Local Culture Research and Design Innovation Teacher Team": A Project among Guangxi-Colleges Key Laboratory of Big Data for Innovative Design.

References

[1] Voulodimos, A., Doulamis, N., Doulamis, A., & Protopapadakis, E. (2018). Deep learning for computer vision: A brief review. Computational intelligence and neuroscience, 2018(1), 7068349.

[2] Khan, A. I., & Al-Habsi, S. (2020). Machine learning in computer vision. Procedia Computer Science, 167, 1444-1451.

[3] Prince, S. J. (2012). Computer vision: models, learning, and inference. Cambridge University Press.

[4] Ikeuchi, K. (Ed.). (2021). Computer vision: A reference guide. Cham: Springer International Publishing.

[5] Nigel, F., & Liliya, K. (2014). Past and future applications of 3-D (virtual reality) technology. Научно-технический вестник информационных технологий, механики и оптики, (6 (94)), 1-8.

[6] Lanier, J. (2017). Dawn of the new everything: Encounters with reality and virtual reality. Henry Holt and Company.

[7] Earnshaw, R. A. (Ed.). (2014). Virtual reality systems. Academic press.

[8] Deshmukh, S. S., & Goswami, A. (2021). Recent developments in hot embossing–a review. Materials and Manufacturing Processes, 36(5), 501-543.

[9] Bhandari, A., Khatri, N., Mishra, Y. K., & Goyat, M. S. (2023). Superhydrophobic coatings by the hot embossing approach: recent developments and state-of-art applications. Materials Today Chemistry, 30, 101553.

[10] Velten, T., Bauerfeld, F., Schuck, H., Scherbaum, S., Landesberger, C., & Bock, K. (2011). Roll-to-roll hot embossing of microstructures. Microsystem technologies, 17, 619-627.

[11] Al-Rubaie, R. M. H. (2021). Embossing technologies and their role in enhancing the aesthetic dimension of digital printing. Al-Academy, (101), 5-20.

[12] Deshmukh, S. S., & Goswami, A. (2022). Current innovations in roller embossing—A comprehensive review. Microsystem Technologies, 28(5), 1077-1114.

[13] Feldmann, J., Braig, F., Spiehl, D., Dörsam, E., & Blaeser, A. (2022). Generation of a paper embossing preview using 3D scanning and Fourier analysis. Advances in Printing and Media Technology, 48, 177-187.

[14] Nguyen, L., Wu, M. H., & Hung, C. (2019). Finite element analysis of ultrasonic vibration-assisted microstructure hot glass embossing process. Australian Journal of Mechanical Engineering, 17(3), 199-208.

[15] Tsutsui, A., Fushimi, T., Murakami, T., Kojima, R., Tanaka, K., & Ochiai, Y. (2024, May). HIFU Embossment of Acrylic Sheets. In Proceedings of the CHI Conference on Human Factors in Computing Systems (pp.

1-23).

[16] Bahga, S. S., & Khatait, J. P. (2021). Design of precision hot embossing machine for micropatterning on PMMA. Journal of Micro and Nano-Manufacturing, 9(3).

[17] Gosselin, D., Belgacem, M. N., Joyard-Pitiot, B., Baumlin, J. M., Navarro, F., Chaussy, D., & Berthier, J. (2017). Low-cost embossed-paper micro-channels for spontaneous capillary flow. Sensors and Actuators B: Chemical, 248, 395-401.

[18] Jarczynski, M., Mitra, T., Brüning, S., Du, K., & Jenke, G. (2018, February). Parallel processing of embossing dies with ultrafast lasers. In Laser-based Micro-and Nanoprocessing XII (Vol. 10520, pp. 79-88). SPIE.

[19] Edwards, M. (2016). A Guide to Modelling in Clay and Wax: And for Terra Cotta, Bronze and Silver Chasing and Embossing, Carving in Marble and Alabaster, Moulding and Casting in Plaster-Of-Paris or Sculptural Art Made Easy for Beginners. Read Books Ltd.

[20] Xingkang Yang,Yang Li,Dianlong Li,Shaolong Wang & Zhe Yang. (2024). Siam-AUnet: An end-to-end infrared and visible image fusion network based on gray histogram. Infrared Physics and Technology105488-105488.

[21] Genlang Chen,Han Zhou,Gang Huang,Guanghui Song & Jiajian Zhang. (2023). A deep image segmentation-based method for stitching ancient-book images without an overlapping region. IET Image Processing(10),3068-3078.

[22] Boran Jiang,Ping Wang,Shuo Zhuang,Maosong Li,Zhenfa Li & Zhihong Gong. (2018). Detection of maize drought based on texture and morphological features. Computers and Electronics in Agriculture50-60.

[23] Iqbal Naveed,Mumtaz Rafia,Shafi Uferah & Zaidi Syed Mohammad Hassan. (2021). Gray level co-occurrence matrix (GLCM) texture based crop classification using low altitude remote sensing platforms..PeerJ. Computer sciencee536-e536.

[24] Chunmeng Liu,Jiang Zhou & Changjiang Bu. (2024). The high order spectral extremal results for graphs and their applications. Discrete Applied Mathematics209-214.

[25] AliKhan,Md. MoinulHossain,AlexandraCovaci,KonstantinosSirlantzis & ChuanlongXu. (2024). Light field imaging technology for virtual reality content creation: A review. IET Image Processing(11), 2817-2837.